J. Fluid Mech. (1999), *vol.* 382, *pp.* 283–306. Printed in the United Kingdom

Secondary instabilities in rapidly rotating fluids: inertial wave breakdown

By R. R. KERSWELL

Department of Mathematics, University of Bristol, Bristol, BS8 1TW, UK

(Received 9 June 1998)

Inertial waves are a ubiquitous feature of rapidly rotating fluids. Although much is known about their initial excitation, little is understood about their stability. Experiments indicate that they are generically unstable and in many cases catastrophically so, quickly causing the whole flow to collapse to small-scale disorder. The linear stability of two three-dimensional inertial waves observed to break down in the laboratory is considered here at experimentally small but finite Ekman numbers of $\leqslant 10^{-4}$. Surprisingly small threshold amplitudes for instability are found. The results support the conjecture that triad resonances are the generic mechanism for secondary instability in rapidly rotating fluids but also highlight the ability of geostrophic flows to derive energy through a finite-amplitude inertial wave. This latter finding may go some way to explaining the significant mean circulations typically observed in inertial wave experiments.

1. Introduction

It is well known that inertial oscillations with a frequency less than twice the basic rotation frequency can exist within a uniformly and rapidly rotating fluid (Kelvin 1880; Poincaré 1910; Cartan 1922). A large body of literature now exists cataloguing how such modes may either be directly forced (Fultz 1959; Baines 1967; Johnson 1967; Aldridge & Toomre 1969; McEwan 1970; Stergiopoulos & Aldridge 1982, 1987; Rieutord 1991; Manasseh 1992, 1994, 1996; Kobine 1995, 1996; Tilgner 1998) or produced via a bifurcation (Malkus 1968, 1989; Gledzer *et al.* 1974; Gledzer & Ponomarev 1977, 1992; Vladimirov & Tarasov 1985; Vladimirov & Vostretsov 1986; Waleffe 1989; Kerswell 1993, 1994; Aldridge *et al.* 1997; Kerswell & Malkus 1998). The experimental work performed so far has not only largely confirmed linear, inviscid, inertial-wave theory but also clearly suggested that inertial waves are generically unstable above a threshold amplitude. This instability leads to complicated nonlinear behaviour and typically triggers an abrupt breakdown of the whole flow to small-scale disorder christened 'resonant collapse' by McEwan (1970) (Manasseh 1992).

A triad resonance in which two infinitesimal inertial waves form a three-wave interaction with the finite primary wave is certainly the natural candidate for this initial inertial wave instability or secondary bifurcation of the whole flow (e.g. McEwan 1970). The observed resonant collapse phenomenon strongly suggests that the next or tertiary bifurcation leads directly to a strange attractor rather than a three-frequency quasi-periodic motion (Ruelle & Takens 1971; Newhouse, Ruelle & Takens 1978). It has been hypothesized that the presence of large geostrophic flows may be instrumental in this resonant collapse process (McEwan 1970; Kobine 1995). Such

flows and how they are generated are a longstanding issue in rapidly rotating fluid mechanics. It is well known that a small-amplitude inertial wave can only directly drive a mean circulation at second order in its amplitude and then only through the combined influences of nonlinearity and viscosity (Greenspan 1969). However, experimental observations sometimes seem to find larger amplitude geostrophic flows accompanying inertial waves than those which can be understood through formal asymptotic theory (even including the effects of the Ekman boundary layer eruptions – see Hollerbach & Kerswell 1995; Kerswell 1995). It is natural to speculate here that such mean flows may be the direct result of inertial wave instability. Such a secondary 'geostrophic' instability could not be a triad resonance in keeping with Greenspan's (1969) observation.

Motivated by these issues, the purpose of this paper is to perform a linear stability analysis for a three-dimensional, finite-amplitude inertial wave in the presence of small but finite fluid viscosity, $0 < E \ll 1$ (where E is the Ekman number). From the prospective of the rotating fluid as a whole, this can be viewed as a secondary stability analysis assuming that the primary inertial wave instability has saturated at some small amplitude. Closely associated recent work by Lifschitz & Fabijonas (1996) (see also Fabijonas, Holm & Lifschitz 1997) in inviscid, unbounded rotating systems using a geometrical optics technique has shown that standing Kelvin waves are generically unstable to short-wavelength perturbations. Since Kelvin waves are the plane wave equivalent of contained inertial waves, this overall conclusion should carry over in some sense and we seek to confirm that here for small but non-vanishing viscosity. The particular inertial waves chosen, the range of amplitudes and Ekman numbers considered are all motivated by the bifurcations observed in recent experiments involving an elliptically distorted rotating cylinder of fluid (Malkus 1989, 1994; Malkus & Waleffe 1991). In principle, therefore, time series data are available to test the predictions made here. Despite this particular application, the analysis is kept as general as possible by not including the initial generating mechanism for the primary instability; in other words, the underlying basic flow is taken to be uniform rotation without any elliptical distortion. The objectives are essentially threefold. Firstly and most obviously, we want to establish that the inertial waves considered are indeed unstable and to quantify the threshold amplitude for this secondary instability at experimental Ekman numbers of $E \leqslant 10^{-4}$. Secondly, we want to understand the structure of the secondary instability: is it always a triad resonance as conjectured or are geostrophic flows also excitable? The latter would, as mentioned above, have immediate implications for the circulations observed experimentally which do not fit into the second-order framework of asymptotic theory. Finally, we would like to determine whether the preferred (most unstable) secondary instability is robust over changes of the primary wave amplitude A. Experiments do plausibly indicate that the primary wave does saturate long before any secondary instability appears suggesting the quasi-steady stability analysis pursued here. Results which indicate that the most unstable secondary disturbance is the same over the range of relevant amplitudes A would provide some *a posteriori* justification for this approach.

The plan of the paper is as follows. Section 2 introduces the governing equations for a rapidly rotating, incompressible, constant-density fluid contained within a circular cylinder. The structure of the inertial waves (primary instabilities) existant on the underlying basic state of uniform rotation is then discussed before the secondary instability analysis of one such primary wave is described. For small but finite Ekman number, some compromise has to be made on the exact boundary conditions used in the calculations and this is argued for here. Section 3 details the numerical techniques

used and § 4 presents the results which are then discussed in § 5. The Appendix gathers together a relevant pseudo-asymptotic calculation and numerical data on the viscous decay rates of two inertial waves for small but finite Ekman number obtained during the course of the study.

2. Formulation

We consider the motion of a viscous, incompressible, constant-density fluid within a circular cylinder of radius R and height Rd rotating uniformly about its axis at rate Ω. The equations of motion for the fluid velocity in the frame of rotation of the cylinder are

$$\frac{\partial \boldsymbol{u}}{\partial t} + \boldsymbol{u}\cdot\nabla\boldsymbol{u} + 2\widehat{\boldsymbol{k}}\times\boldsymbol{u} + \nabla p = E\nabla^2\boldsymbol{u}, \tag{2.1}$$

$$\nabla\cdot\boldsymbol{u} = 0, \tag{2.2}$$

with boundary conditions

$$\boldsymbol{u} = \boldsymbol{0}|_{\partial V}. \tag{2.3}$$

The basic rotation rate, Ω, cylindrical radius, R, and density, ρ, have been used to non-dimensionalize the system, with the Ekman number $E = \nu/\Omega R^2$ appearing as the non-dimensionalization of the kinematic viscosity ν.

2.1. *Primary instability: inertial waves*

The inviscid and small velocity limits give rise to the well known inertial wave problem (Greenspan 1968)

$$\frac{\partial \boldsymbol{u}}{\partial t} + 2\widehat{\boldsymbol{k}}\times\boldsymbol{u} + \nabla p = \boldsymbol{0}, \tag{2.4}$$

$$\nabla\cdot\boldsymbol{u} = 0, \tag{2.5}$$

with reduced boundary conditions

$$\boldsymbol{u}\cdot\widehat{\boldsymbol{n}} = 0|_{\partial V}. \tag{2.6}$$

This is the underlying homogeneous problem which defines the neutral normal modes of oscillation of a contained rotating fluid and is the basis for understanding the primary instability of an almost uniformly rotating fluid (e.g. Kelvin 1880; Fultz 1959; Wood 1966; Johnson 1967; Greenspan 1968; McEwan 1970). Separable solutions exist (Greenspan 1968) of the form

$$\boldsymbol{u} = \begin{bmatrix} \frac{1}{2}\mathrm{i}\{(\lambda+2)J_{m-1}(ks) - (\lambda-2)J_{m+1}(ks)\}\cos(l\pi z/d) \\ -\frac{1}{2}\{(\lambda+2)J_{m-1}(ks) + (\lambda-2)J_{m+1}(ks)\}\cos(l\pi z/d) \\ \mathrm{i}\lambda kd(\pi l)^{-1}J_m(ks)\,\sin(l\pi z/d) \end{bmatrix} \mathrm{e}^{\mathrm{i}(m\phi+\lambda t)}, \tag{2.7}$$

$$p = -\frac{1}{k}J_m(ks)\,\cos(l\pi z/d)\,\mathrm{e}^{\mathrm{i}(m\phi+\lambda t)}, \tag{2.8}$$

in cylindrical coordinates (s, ϕ, z) where

$$\lambda = \frac{\pm 2}{(1 + k^2d^2/(\pi l)^2)^{1/2}},$$

and k is a solution, indexed by n such that $0 < k_{n=1} < k_{n=2} \ldots$, of

$$s\frac{\mathrm{d}}{\mathrm{d}s}J_m(ks) + \frac{2m}{\lambda}J_m(ks) = 0|_{s=1}.$$

Three numbers, l, $n \in \mathbb{N}$, and $m \in \mathbb{Z}$, are sufficient to specify the inertial mode and in particular the frequency $\lambda = \lambda_{lmn}$. These indices correspond roughly with the number of nodes axially, radially, and azimuthally respectively in the pressure eigenfunction.

2.2. *Secondary instability*

In order to study the prevalence of secondary instabilities, we focus on two particular inertial waves which are easily excited in the laboratory through the elliptical instability (Malkus 1989, 1994; Malkus & Waleffe 1991) and therefore for which there are experimental data. Generically, the elliptical instability manifests itself through the resonant growth of two different inertial waves which form a resonant triad with the underlying 'wave' of elliptical distortion. A relatively simple 'subharmonic' instability arises when the two inertial waves excited are complex conjugates of each other (Kerswell 1994). For this to be the dominant instability, an inertial wave with azimuthal wavenumber $m = 1$ must be tuned by varying the cylinder height d until its frequency in the rotating frame, λ, is sufficiently close to 1 (where the definition here of 'closeness' depends on the fluid's viscosity). Two experimental configurations in which these subharmonic elliptical instabilities have been observed are cylinders of height $d = 1.9121$ and $d = 3.9796$. The excited inertial wave in each of these two cases is uniquely defined by the azimuthal, axial and radial wavenumbers, $m = 1$, $\alpha = 2\pi/d$ and $k = \sqrt{3}\alpha$, and d is such that the frequency $\lambda = 1$ (for $E = 0$). Since $\lambda_{lab} = \lambda - m = 0$, these waves are conveniently steady in the laboratory frame which is therefore the natural frame in which to consider their stability.

Ideally, we would like to study the linear stability of these inertial waves in the experimental regime where the fluid viscosity is small (so the concept of an inertial wave still makes sense) but finite, that is, typically $0 < E \leqslant 10^{-4}$. This, of course, formally requires numerically resolving $E^{1/2}$ Ekman boundary layers on both curved and flat surfaces of the rigid cylindrical container for a general three-dimensional disturbance, which is still not computationally feasible (Kerswell & Barenghi 1995). One drastic approach to this problem is to consider the inviscid stability of the inertial wave, which is well within reach numerically and theoretically appealing. However, the results prove difficult to interpret on their own given that some instabilities will disappear or their growth rates be more severely reduced than others in an non-obvious way under the introduction of viscosity. Therefore, as a necessary compromise, we primarily consider retaining the fluid's viscosity but relax the non-slip boundary conditions on the top and bottom surfaces to those of the stress-free type. This has the effect of reducing an impractical stability analysis into now only a difficult one. Qualitatively, the leading viscous damping of inertial waves is retained at the correct order with their damping rates and frequency shifts remaining $O(E^{1/2})$ although the actual numerical coefficients are obviously reduced somewhat. This is not true, unfortunately, for geostrophic modes whose viscous dissipation occurs dominantly in the non-slip horizontal Ekman boundary layers. The viscous damping for these modes is reduced from $O(E^{1/2})$ to $O(E)$ by the introduction of stress-free boundary conditions. However, the results we obtain below using this reduced model can easily be re-interpreted to take account of this difference. The 'reduced' viscous model has also the considerable benefit of making contact with other current numerical work with similar aims which uses exactly the

same model but is a complementary time-stepping calculation (Mason & Kerswell 1998).

The *inviscid* problem studied in this paper considers the linear stability of the steady flow

$$\boldsymbol{U} = s\widehat{\boldsymbol{\phi}} + A\begin{bmatrix} -\{3J_0(ks) + J_2(ks)\}\sin\phi\cos\alpha z \\ -\{3J_0(ks) - J_2(ks)\}\cos\phi\cos\alpha z \\ -2\sqrt{3}J_1(ks)\sin\phi\sin\alpha z \end{bmatrix} + O(A^2) \tag{2.9}$$

in the laboratory frame as a function of A for the two inertial waves of interest. To make the subsequent stability calculation as general as possible, the generating mechanism for the inertial wave was not included. In other words, we assume that the inertial wave has been excited to some saturation amplitude where it is maintained. This amplitude A of the inertial wave is assumed small (in fact $A \leqslant 0.075$ throughout for $E \leqslant 10^{-4}$) so that the $O(A^2)$ terms can be ignored. Of course, the leading-order corrections, the second-harmonic and mean-flow terms, are calculable and can be included for more completeness but this was not attempted here. These terms will lead to different triad resonances with $O(A)$ smaller growth rates than those produced by the leading $O(A)$ inertial wave. Interestingly, experimental data show these inertial waves appearing to maintain their identity up to amplitudes of $A \approx 0.1$ – see figure 1 – which tends to support this simple-minded approach. For the *viscous* stability analysis the viscous analogue of this basic flow (2.9) was obtained numerically by solving the appropriate 'primary' eigenvalue problem normalized such that $u(0, \phi, z) = -3A\ \sin\ \phi\ \cos\ \alpha z$ to be consistent with (2.9). The addition of viscosity, of course, acts to slightly modify the frequency of the inertial wave by an $O(E^{1/2})$ amount. Formally, we should move into a correspondingly slowly rotating frame to retain steadiness of the inertial mode and proceed from there. However, for our purposes this is a needless complication which will only act to recalibrate things very slightly. To simplify matters, we imagine that the cylinder height d and hence the axial wavelength have changed by $O(E^{1/2})$ to precisely compensate for the viscous frequency shift. This is after all how the instability is achieved experimentally.

The linearized viscous equations are

$$\frac{\partial \boldsymbol{u}}{\partial t} + \boldsymbol{U}\cdot\nabla\boldsymbol{u} + \boldsymbol{u}\cdot\nabla\boldsymbol{U} + \nabla p = E\nabla^2\boldsymbol{u}, \tag{2.10}$$

$$\nabla\cdot\boldsymbol{u} = 0, \tag{2.11}$$

subject to non-slip conditions at the sides and stress-free conditions at the top and bottom surfaces,

$$\boldsymbol{u} = \boldsymbol{0}, \quad s = 1; \quad \boldsymbol{u}\cdot\widehat{\boldsymbol{z}} = 0, \quad \frac{\partial}{\partial z}(\widehat{\boldsymbol{z}}\times\boldsymbol{u}) = \boldsymbol{0}, \quad z = 0,\ d. \tag{2.12}$$

Separating the time dependence by the usual ansatz $\boldsymbol{u}(\boldsymbol{x}, t) = \boldsymbol{u}(\boldsymbol{x})\,\mathrm{e}^{\sigma t}$ converts the problem (2.10)–(2.12) into an eigenvalue problem for σ with $\mathrm{Re}(\sigma) > 0$ indicating linear instability. One of the aims of the calculation was to learn how large A could be as a function of E before an inertial wave loses stability. The particular features of note here are that the basic state is three-dimensional and parametrized by the free amplitude of the inertial wave in addition to the Ekman number in the viscous case, $\boldsymbol{U} = \boldsymbol{U}(s, \phi, z; A, E)$. Only the special form of the ϕ and z dependence of $\boldsymbol{U}$ coupled with $A \ll 1$ rendered the eigenvalue problem numerically feasible at small E.

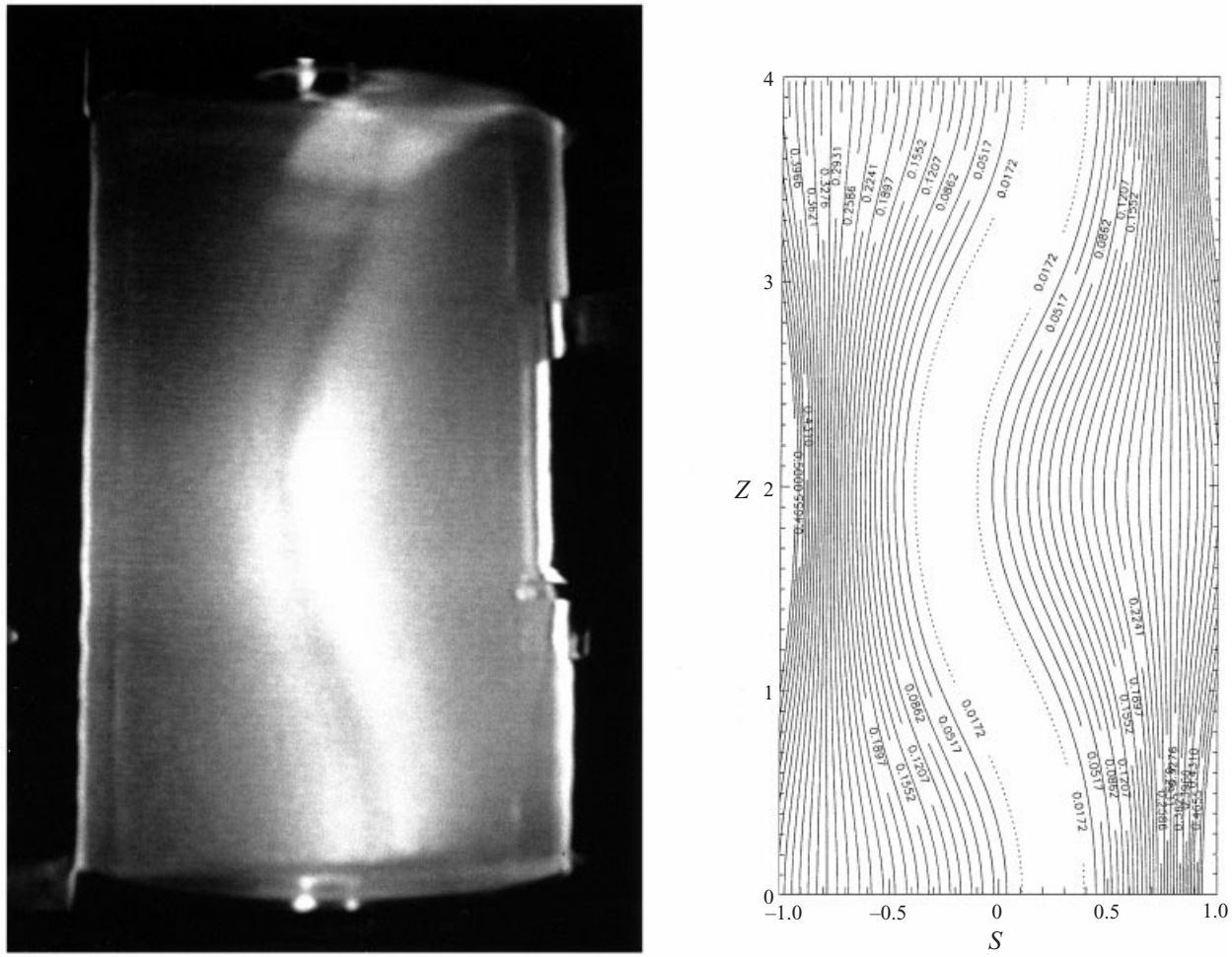

FIGURE 1. A photograph of the elliptically excited inertial wave $m = \lambda_{rot} = 1$, $l = 2$ for a cylinder of height-to-radius ratio $d = 3.9796$ (Malkus 1989, 1994). The dark snaking central line is thought to represent the perturbed rotation axis of the flow. A contour plot of the kinetic energy density alongside for $A = 0.1$ in (2.9) gives a reasonable image of this flow. (The deflection of the fluid's rotation axis from the cylinder's axis of symmetry is directly proportional to A.)

3. Numerics

The problem (2.10)–(2.12) was solved as stated – 3 momentum + 1 continuity equations – in terms of the primitive variables (u, v, w, p) rather than any reduced representation of the velocity field such as a poloidal–toroidal decomposition. Experience indicates that the subsequent eigenvalue problem tends to have more stable convergence properties and less spurious eigenvalues (Kerswell & Davey 1996). The equations were imposed by collocation in s, and Galerkin projection in both ϕ and z. The latter was used to exploit the limited banded structure of the discretization matrices so that an inverse iteration scheme was also available in addition to the standard generalized eigenvalue approach. This crucially allowed eigenvalues necessarily calculated at great cost by using a generalized eigenvalue algorithm to be checked for convergence and 'polished' to greater accuracy.

Computationally, rather than viewing the interior of the cylinder as the region $\{0 \leqslant s \leqslant 1, -\pi \leqslant \phi < \pi\}$, we consider the equivalent domain $\{-1 \leqslant s \leqslant 1, 0 \leqslant \phi < \pi\}$. The solution in $-1 \leqslant s < 0$ can be constructed from that in $0 < s \leqslant 1$ through the known symmetries of the cylindrical polar coordinate system (for example if m is odd, u is an even function of s – see the appendix of Kerswell & Davey 1996) and so we need only collocate the equations over the positive zeros of the $2N$th Chebyshev polynomial $T_{2N}(s) = \cos(2N \cos^{-1} s)$. Boundary conditions need then only be imposed at $s = 1$ which is easily built-in to each spectral expansion function. This approach is in contrast to the normal technique of expanding in modified Chebyshev polynomials $T_n(2s-1)$, $n = 0, 1, 2, \ldots, N$, collocating over, say, the Gauss–Lobatto points $s_j = \frac{1}{2}(\cos[j\pi/(N-1)] + 1)$, $j = 1, 2, \ldots, N-1$ (e.g. O'Sullivan & Breuer 1994) and explicitly imposing the regularity conditions

$$(m \pm 1)(\mathrm{i}u \mp v) = \mathrm{i}mw = \mathrm{i}mp = 0 \tag{3.1}$$

at the axis. By building the appropriate radial parities into the expansions, the correct axial behaviour automatically follows without need to explicitly impose the regularity conditions (3.1). Most important of all, however, is that this prescription which exploits the symmetries in s concentrates the collocation points entirely near $s = 1$ exactly where the Ekman boundary layer must be resolved. The spectral expansions for the solutions sought are

$$\left.\begin{aligned} \boldsymbol{u} &= \sum_{n=0}^{N-1} \sum_{m=M0}^{M+M0} \sum_{l=0}^{L} \begin{bmatrix} u_{nml} U_n^{(m)}(s) \cos[(l+\Delta)\alpha z] \\ v_{nml} V_n^{(m)}(s) \cos[(l+\Delta)\alpha z] \\ w_{nml} W_n^{(m)}(s) \sin[(l+\Delta)\alpha z] \end{bmatrix} \mathrm{e}^{\mathrm{i}m\phi+\sigma t}, \\ p &= \sum_{n=0}^{N-1} \sum_{m=M0}^{M+M0} \sum_{l=0}^{L} p_{nml}\, P_n^{(m)}(s) \cos[(l+\Delta)\alpha z]\, \mathrm{e}^{\mathrm{i}m\phi+\sigma t} \end{aligned}\right\} \tag{3.2}$$

where $\Delta = 0$ or $\frac{1}{2}$ (recall that $\alpha = 2\pi/d$) and the boundary conditions are implicitly built-in to the spectral functions,

$$[U_n^{(m)}(s),\, V_n^{(m)}(s),\, W_n^{(m)}(s),\, P_n^{(m)}(s)] = \begin{cases} [\Theta_{2n+3}(s),\, \Theta_{2n+3}(s),\, \Theta_{2n+2}(s),\, T_{2n}(s)], & m \text{ even} \\ [\Theta_{2n+2}(s),\, \Theta_{2n+2}(s),\, \Theta_{2n+3}(s),\, T_{2n+1}(s)], & m \text{ odd} \end{cases}$$

and in the inviscid case

$$[U_n^{(m)}(s),\ V_n^{(m)}(s),\ W_n^{(m)}(s),\ P_n^{(m)}(s)] = \begin{cases} [\Theta_{2n+3}(s),\ T_{2n+1}(s),\ T_{2n}(s),\ T_{2n}(s)], & m \text{ even} \\ [\Theta_{2n+2}(s),\ T_{2n}(s),\ T_{2n+1}(s),\ T_{2n+1}(s)], & m \text{ odd} \end{cases}$$

with $\Theta_n(s) = T_n(s) - T_{n-2}(s)$. (Note when $\Delta = 0$ $w_{nm0} = 0\ \forall n, m$, $u_{n00} = 0\ \forall n$ and $p_{000} = 0$.) Implicit in the representation (3.2) is the fact that the value of Δ partitions the eigensolutions into two different families which either have complete axial wavelengths enclosed within the cylinder ($\Delta = 0$) or an odd number of half-wavelengths ($\Delta = \frac{1}{2}$). Additionally, since $\boldsymbol{U}$ (only) contains components proportional to $e^{\pm i(\phi+\alpha z)}$ and $e^{\pm i(\phi-\alpha z)}$, the $\Delta = 0$ family can be further subdivided into eigensolutions where $l+m$ is even and eigenfunctions where $l+m$ is odd. In summary we may examine linear stability by solving for the three families separately

$$1.\quad \Delta = 0,\ l+m \text{ is even}, \quad 2.\ \Delta = 0,\ l+m \text{ is odd}, \quad 3.\ \Delta = \tfrac{1}{2}. \tag{3.3}$$

These will be referred to as modes 1, 2 and 3 hereafter. Since $l + \Delta$ can only be zero for $\Delta = 0$, geostrophic flow instabilities are either of mode type 1 or 2: mode 3 instabilities must be triads.

It is tempting to simplify the calculation further by considering the travelling wave analogue of the standing inertial wave in an infinite cylinder. The basic flow would then only have components $e^{\pm i(\phi+\alpha z)}$ or $e^{\pm i(\phi-\alpha z)}$ and the stability analysis would then be a much easier two-dimensional computation. However, these results would only be useful if the dominant instabilities realized in the full three-dimensional system are essentially two-dimensional in the parameter range of interest. Experience showed this only to be true for very small Ekman numbers $E \leqslant 10^{-5.5}$ (see below).

4. Results

Numerically, the search for secondary instabilities proceeds by systematically sweeping across the two-dimensional azimuthal–axial wavenumber space with given truncations M and L to find all unstable eigenfunctions. The inclusion of viscosity, which acts to dampen preferentially the high-wavenumber modes, crucially allows attention to be focused on the small wavenumbers. Additionally, an initial search quickly indicates that the growing modes are invariably located in the very low axial wavenumber range. This motivated the expansions used in (3.2) which are built to start at the lowest possible axial wavenumber. In contrast, the azimuthal wavenumber 'origin' $M0$ must be varied to capture all the important instabilities.

A priori, it is not clear what parameter range in (A, E) space is accessible to this procedure given equipment limits in speed and memory. The initial identification of instabilities has to be done using an eigenvalue code which using a truncation $[N, M, L]$ has storage requirements $O(N^2M^2L^2)$. The truncation in M and L must be large enough to capture all the Fourier modes coupled together into an eigenfunction yet small enough to allow enough radial truncation to resolve the Ekman boundary layers of each Fourier mode. One obvious limiting scenario is E becoming too small, forcing the radial truncation N to increase more than the product ML can be reduced as A_{crit} also decreases. The other is E becoming too large, forcing A_{crit} and hence ML to increase faster than N decreases. Fortunately, an initial investigation revealed that secondary instabilities at experimental Ekman numbers of 10^{-5} to 10^{-4} are resolvable using a 300MB Ultraspark workstation. The search over $M0$ was started at $M0 = -3$

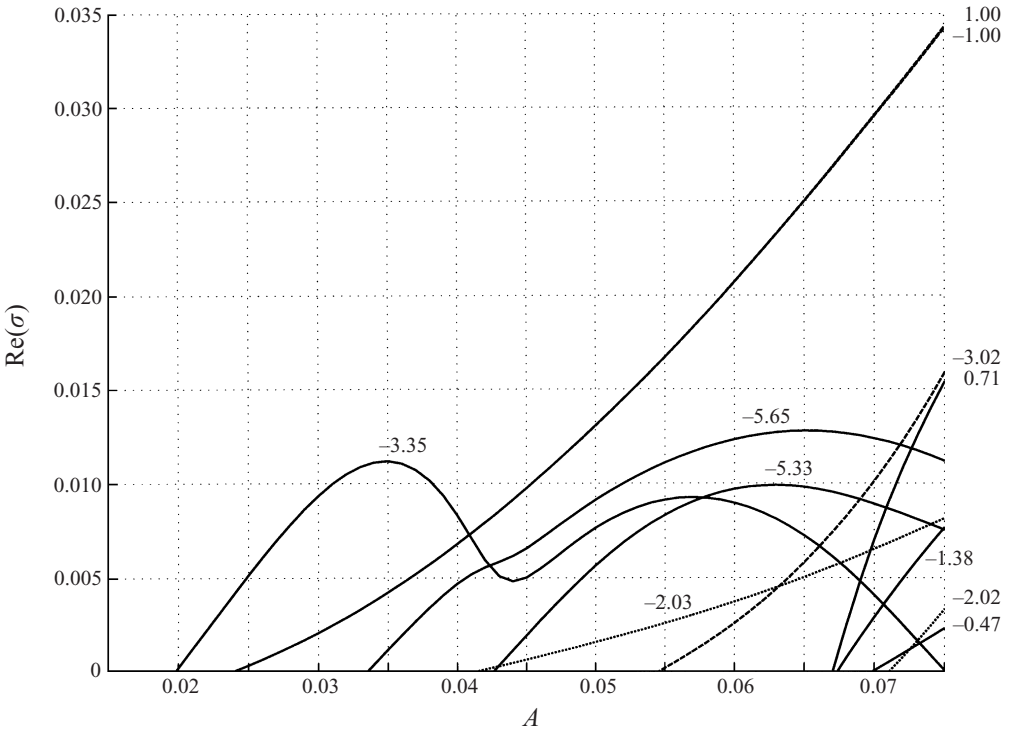

FIGURE 2. The growth rates of secondary instabilities plotted against amplitude of the underlying inertial wave for the inertial wave with $m = 1, l = 2$ in $d = 1.9121$ at $E = 10^{-4}$. The dotted line indicates modes of type 1, dashed line modes of type 2, and the solid line modes of type 3. Each line is also labelled with a representative frequency (this of course varies slightly with A). The inertial wave is unstable when its amplitude exceeds ≈ 0.02.

and then concentrated on positive $m \leqslant 10$. This is sufficient to capture all instabilities over the range $-10 \leqslant m \leqslant 10$ since any eigenfunction has a complex conjugate partner found by reflecting in $m = 0$ for $\Delta = 0$ or $m = \frac{1}{2}$ for $\Delta = \frac{1}{2}$. Typical truncations for the full eigenvalue code were $[25, 7, 5]$ (using the notation $[\tilde{N}, M, L]$) for modes 1 and 2 of (3.3) and $[25, 6, 3]$ for mode 3. Unstable eigenfunctions were verified and 'polished' using an inverse iteration code which exploited the finite bandwidth in m. Typical truncation levels for this were $[40, 6, 5]$ to $[30, 9, 7]$ for modes 1 and 2, and $[30, 7, 3]$ to $[20, 5, 5]$ for mode 3. All growth rates were resolved to at least 2 significant figures.

4.1. $d = 1.9121$, $E = 10^{-4}$

Figure 2 shows that the inertial wave with $\lambda = m = 1$, $l = 2$ in a container of height-to-radius ratio of 1.9121 is unstable when its amplitude (as defined in (2.9)) exceeds 0.02 at $E = 10^{-4}$. Initially, the most rapidly growing instability has a frequency of ≈ -3.35 until at $A \approx 0.04$ it is surpassed by *two* modes of almost identical growth rates who have frequencies of $\approx \pm 1.00$ (In fact, by an amplitude of $A = 0.075$, the first instability is now completely stabilized.) The $(m, \ell = l + \Delta)$ structures of these modes are illustrated in table 1(a–c) which are in effect two-dimensional spectra. The numbers shown there (and in other later tables of the same form) indicate how the energy of the eigenfunction is distributed amongst the constitutive Fourier modes. This helps to identify the character of the instability. For example, the -3.35 initial instability, table 1(a), is clearly the result of a three-

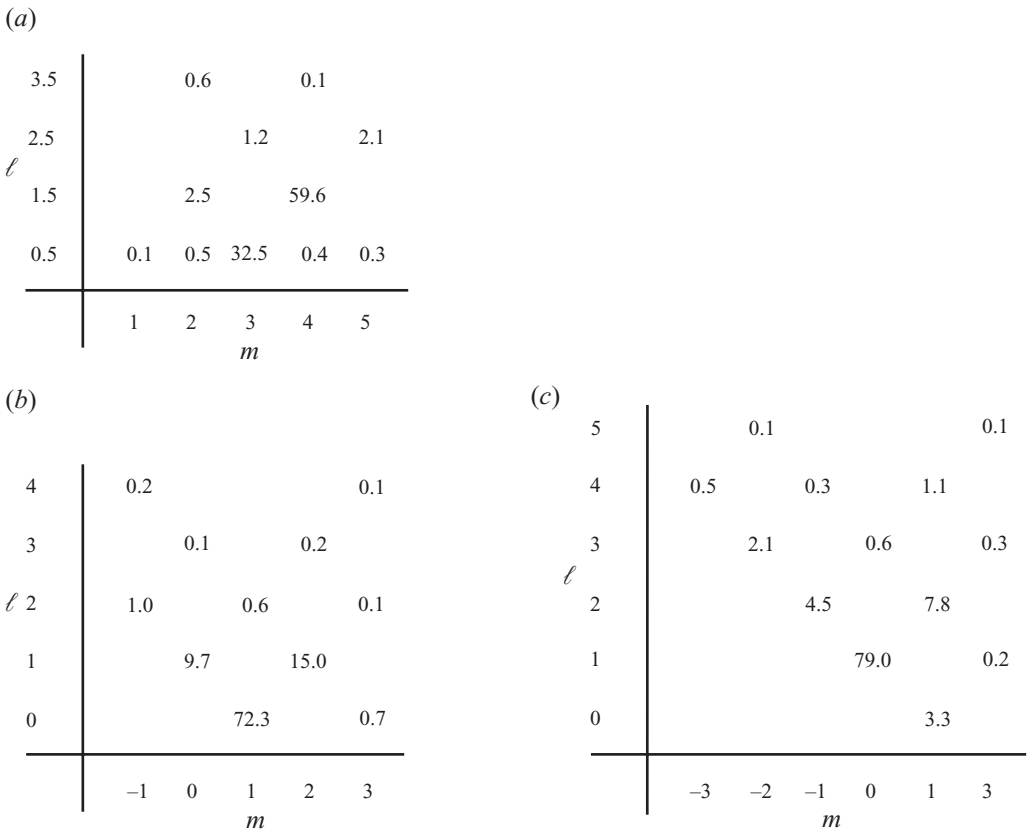

TABLE 1. The structure of the instabilities at $d = 1.9121$ and $E = 10^{-4}$. The number shown at $(m, \ell = l + \Delta)$ is the percentage of the total modal energy contained within that Fourier constituent of the eigenfunction (only energies which are larger than 0.05% are shown). The instabilities are (*a*) $\sigma = (0.11 \times 10^{-1}, -3.337)$ (truncation $[30, 5, 3]$ $M0 = 1$) at $A = 0.035$ (truncations $[35, 5, 2]$ and $[20, 5, 4]$ also give that the growth rate is 0.11×10^{-1} to 2 significant figures), (*b*) $\sigma = (0.342 \times 10^{-1}, -1.0036)$ (truncation $[30, 8, 5]$ $M0 = -3$) at $A = 0.075$, and (*c*) $\sigma = (0.343 \times 10^{-1}, 1.0036)$ (truncation $[25, 7, 7]$ $M0 = -4$) at $A = 0.075$.

wave resonance between the finite-amplitude inertial wave and inertial modes with (m, ℓ) values of $(3, \frac{1}{2})$ and $(4, \frac{3}{2})$. The instability with frequency ≈ -1, table 1(*b*), is predominantly a geostrophic flow (z-independent) essentially *steady* in the rotating frame, whereas the instability with frequency ≈ 1, table 1(*c*), looks to be effectively axisymmetric and to have the same axial wavelength as the underlying inertial wave.

The instability with dominant geostrophic component is clearly not a triad-type instability since it is straightforward to prove that a geostrophic flow cannot form a resonant triad with two inertial waves (Greenspan 1969). This is particularly easy to see in the cylindrical setting. Consider two inertial waves

$$\boldsymbol{u}_{\pm} = \widehat{\boldsymbol{u}}_{\pm}(s, \phi)\, \mathrm{e}^{\pm \mathrm{i}(\alpha z + \lambda t)} \tag{4.1}$$

which satisfy the inertial wave equation

$$\pm \mathrm{i}\lambda \boldsymbol{u}_{\pm} + 2\widehat{\boldsymbol{k}}\times\boldsymbol{u}_{\pm} + \nabla p_{\pm} = \boldsymbol{0}. \tag{4.2}$$

The curl of (4.2) implies that $\nabla\times\boldsymbol{u}_{\pm} = (2\alpha/\lambda)\,\boldsymbol{u}_{\pm}$ which means that the interaction between these two waves which could possibly drive a geostrophic flow in fact vanishes identically,

$$\boldsymbol{u}_{+}\times(\nabla\times\boldsymbol{u}_{-}) + \boldsymbol{u}_{-}\times(\nabla\times\boldsymbol{u}_{+}) = \boldsymbol{0}. \tag{4.3}$$

Instead, the geostrophic component must be the sole leading term in an asymptotic expansion for $A \to 0$ of the following form:

$$\boldsymbol{u} = \mathrm{e}^{A^2\sigma t}\left[\widehat{\boldsymbol{u}}_G(s)\,\mathrm{e}^{\mathrm{i}m\phi} + A\sum_{j,k=\pm 1}\widehat{\boldsymbol{u}}_{jk}(s)\,\mathrm{e}^{\mathrm{i}[m+j]\phi+\mathrm{i}k\alpha z+\mathrm{i}j\lambda t} + A^2\widehat{\boldsymbol{v}}_G(s)\,\mathrm{e}^{\mathrm{i}m\phi} + \cdots\right] \tag{4.4}$$

in the rotating frame where we assume a geostrophic component of azimuthal wavenumber m, σ is the (possibly complex) growth rate on a $O(1/A^2)$ timescale and λ is the underlying inertial wave frequency (= 1 in this paper). To lowest order, the geostrophic balance for $\boldsymbol{u}_G(s,\phi) = \widehat{\boldsymbol{u}}_G(s)\,\mathrm{e}^{\mathrm{i}m\phi}$ is

$$2\widehat{\boldsymbol{k}}\times\boldsymbol{u}_G + \nabla p_G = \boldsymbol{0}, \tag{4.5}$$

which has solution $\boldsymbol{u}_G = \frac{1}{2}\widehat{\boldsymbol{k}}\times\nabla p_G$ where $p_G = \widehat{p}_G(s)\,\mathrm{e}^{\mathrm{i}m\phi}$ and $\widehat{p}_G(s)$ is an arbitrary function which vanishes at $s = 1$. At next order, we have the forced equations

$$\mathrm{i}j\lambda\boldsymbol{u}_{jk} + 2\widehat{\boldsymbol{k}}\times\boldsymbol{u}_{jk} + \nabla p_{jk} = \boldsymbol{U}_{jk}\times(\nabla\times\boldsymbol{u}_G) + \boldsymbol{u}_G\times(\nabla\times\boldsymbol{U}_{jk}), \quad j,k = \pm 1, \tag{4.6}$$

where $\boldsymbol{U}_{jk}$ is the $\mathrm{e}^{\mathrm{i}(j\phi+k\alpha z+j\lambda t)}$ component of the underlying flow (2.9) at $O(A)$ *in the rotating frame* and $\boldsymbol{u}_{jk}(s,\phi,t) = \widehat{\boldsymbol{u}}_{jk}(s)\,\mathrm{e}^{\mathrm{i}(m+j)\phi+\mathrm{i}k\alpha z+\mathrm{i}j\lambda t}$. At second order in A, we have

$$2\widehat{\boldsymbol{k}}\times\boldsymbol{v}_G + \nabla P_G = \sum_{j,k=\pm 1}\boldsymbol{U}_{jk}\times(\nabla\times\boldsymbol{u}_{-j-k}) + \boldsymbol{u}_{-j-k}\times(\nabla\times\boldsymbol{U}_{jk}) - \sigma\boldsymbol{u}_G, \tag{4.7}$$

where $\boldsymbol{v}_G(s,\phi) = \widehat{\boldsymbol{v}}_G(s)\,\mathrm{e}^{\mathrm{i}m\phi}$. The condition for this equation to have a solution is that $\widehat{\boldsymbol{k}}\cdot\nabla\times$RHS of (4.7) should vanish. This is a linear eigenvalue problem for $p_G(s)$ with eigenvalue σ. Numerically solving this at $E = 0$ and $A = 0.075$ confirms that $\mathrm{Re}(\sigma)$ is $+0.046$ for the geostrophic instability shown in figure 2. This growth rate is reduced to $+0.034$ at $E = 10^{-4}$ albeit with stress-free boundary conditions: realistic non-slip conditions would dampen the instability further. At $E = 10^{-5}$ and $A = 0.02$, 97.2% of the modal energy is observed to reside within the geostrophic component rather than just 72.3% at $E = 10^{-4}$ and $A = 0.075$ consistent with this theoretical picture. Furthermore, since the (inviscid) geostrophic growth rates are $O(A^2)$, we can anticipate that the threshold amplitude, A_{crit}, for instability should scale as $O(E^{1/2})$ or $O(E^{1/4})$ depending on whether the boundary conditions on the top and bottom cylindrical surfaces are stress-free or non-slip respectively. Figure 3 provides a dramatic confirmation of the scaling $A_{crit} = O(E^{1/2})$ in the particular case of the geostrophic instability isolated here. (Figure 4 indicates the convergence with radial truncation for this instability at $E = 10^{-6}$ and $A = 10^{-2.7}$.)

It should be emphasized that since the (inviscid) geostrophic growth rates are $O(A^2)$, this instability appears asymptotically subdominant to the perfectly tuned triad growth rates which are $O(A)$ (see § 5). However, the fact that A is finite in laboratory and numerical experiments, that large numerical coefficients may prefix these growth rate scalings and that the triads may be imperfectly tuned all can potentially overturn this situation. Indeed, we see this in figure 2.

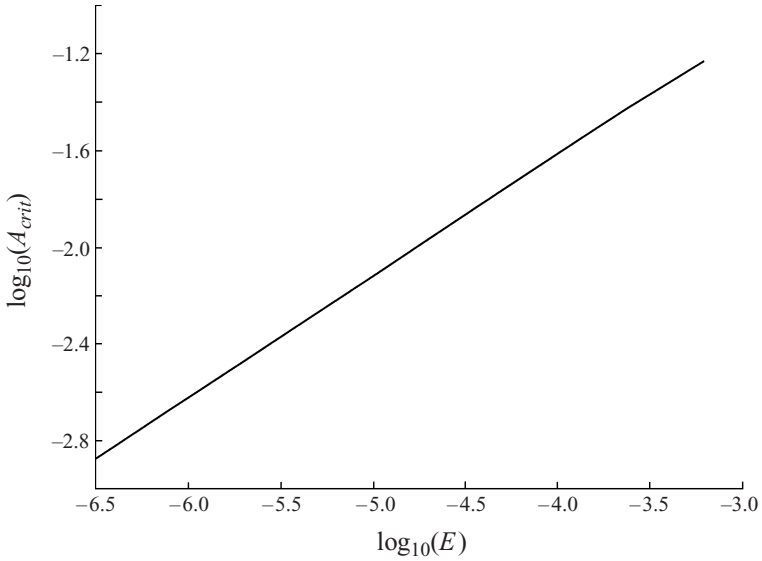

FIGURE 3. A log-log plot of how the critical amplitude for instability, A_{crit}, varies with the Ekman number E for the geostrophic instability of figure 4(b) ($d = 1.9121$). The slope of the line is remarkably constant at 0.5 ± 0.001 confirming the asymptotic prediction $A_{crit} = O(E^{1/2})$.

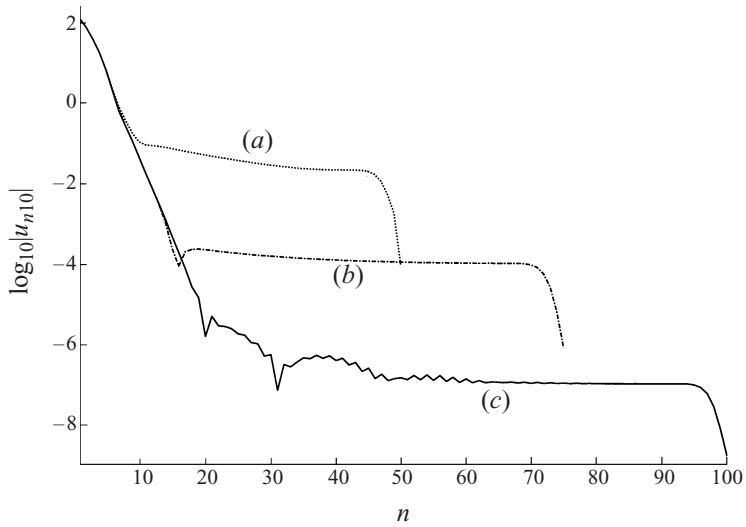

FIGURE 4. Convergence with radial truncation is illustrated here for the geostrophic instability. The absolute value of the spectral coefficients of the radial velocity component, $|u_{n10}|$ (see (3.2)), are plotted on a log scale against spectral degree n at $E = 10^{-6}$ and $A = 10^{-2.7}$ for truncations (a) $N = 100$ (solid), (b) $N = 75$ (dash-dot) and (c) $N = 50$ (dotted). Associated eigenvalues are as follows:

N	$\mathrm{Im}(\sigma)$	$\mathrm{Re}(\sigma)$
100	-0.999992	-0.996523×10^{-5}
75	-0.999992	-0.996520×10^{-5}
50	-0.999992	-0.991621×10^{-5}

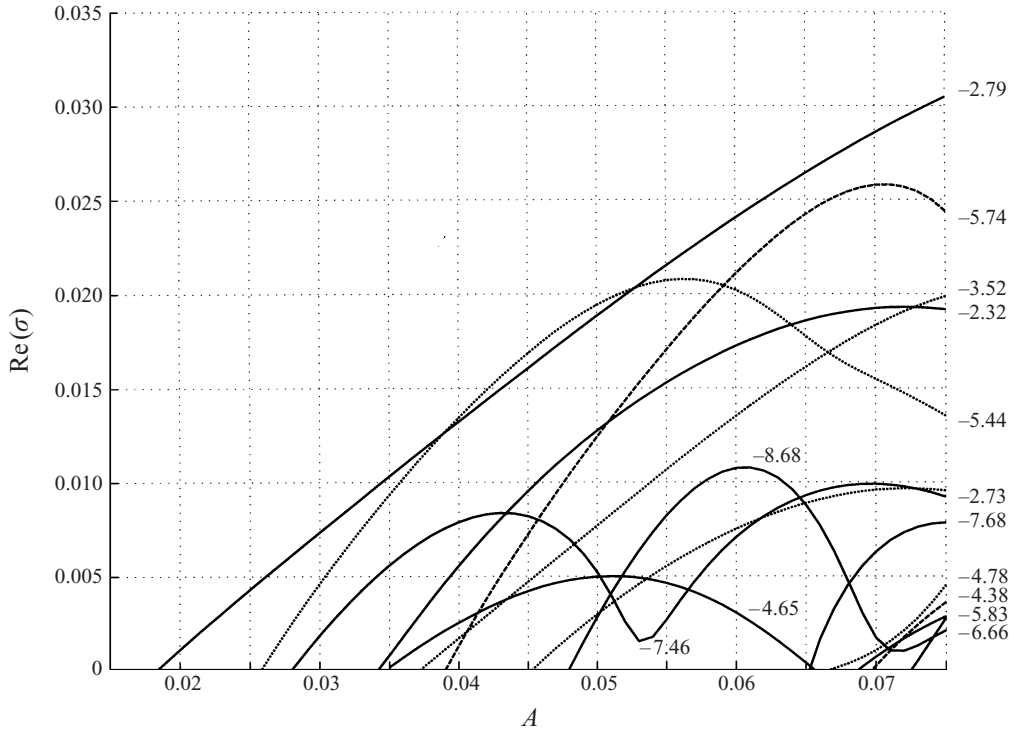

FIGURE 5. The growth rates of secondary instabilities plotted against amplitude of the underlying inertial wave for the inertial wave with $m = 1, l = 2$ in $d = 3.9796$ at $E = 10^{-4}$. The dotted line indicates modes of type 1, dashed line modes of type 2, and the solid line modes of type 3. Each line is also labelled with a representative frequency which varies slightly with A. Again the inertial wave is unstable when its amplitude exceeds ≈ 0.02.

The possibility that geostrophic flows can grow on an inertial wave is extremely noteworthy since the precise generative mechanism for experimentally observed mean (time-averaged in the rotating frame) flows remains a recurring issue (Fultz 1959; Malkus 1968; McEwan 1970; Manasseh 1992, 1994, 1996; Kobine 1995, 1996). Work by Busse (1968) and Greenspan (1969) points towards a combination of viscous and nonlinear effects in the Ekman boundary layer driving these flows directly (see also Kerswell 1995). In this case, the steady (relative to the rotating frame) flow produced must be strictly second order in the amplitude A of the primary inertial wave which is not always convincingly borne out in experiments. The possibility of a secondary 'geostrophic' instability immediately removes this strict $O(A^2)$ expectation for the size of the mean flow. Instead, for example, one could naively anticipate potentially much larger saturation amplitudes for the mean flow (presuming they exist) which scale as the square root of the initial growth rate, $\beta A - \nu E^{1/2}$, where β and ν are $O(1)$ numbers representing the 'inviscid' growth rate and viscous decay rate respectively.

4.2. $d = 3.9796$, $E = 10^{-4}$ *and* 10^{-5}

Figure 5 illustrates the stability situation for the inertial wave $\lambda = m = 1$, $l = 2$ in the cylinder of height-to-radius ratio 3.9796 at $E = 10^{-4}$. Again, the inertial wave is unstable by an amplitude of $A = 0.02$ to a mode 3 instability which this time has a frequency ≈ -2.79. Table 2 indicates that this is a triad instability between the underlying finite-amplitude inertial wave and inertial waves with $(m, \ell) = (2, \frac{3}{2})$ and

$E = 10^{-4}$ $A = 0.075$ $\sigma = (0.30 \times 10^{-1}, -2.79)$

ℓ \ m	0	1	2	3	4
3.5	0.2		0.1		0.1
2.5		0.9		0.8	
1.5	0.2		62.4	0.1	
0.5		1.4		27.8	0.3

$E = 10^{-4.5}$ $A = 0.05$ $\sigma = (0.24 \times 10^{-1}, -2.76)$

ℓ \ m	1	2	3	4
2.5	2.6		0.3	
1.5		68.8		
0.5	0.6	0.3	27.1	0.1

$E = 10^{-5}$ $A = 0.02$ $\sigma = (0.91 \times 10^{-2}, -2.75)$

ℓ \ m	1	2	3
2.5	0.4		0.1
1.5		72.9	
0.5	0.1	0.1	26.5

$E = 10^{-5.5}$ $A = 0.01$ $\sigma = (0.42 \times 10^{-2}, -2.74)$

ℓ \ m	1	2	3
2.5	0.1		
1.5		73.3	
0.5			26.5

TABLE 2. The structure of the $(2, \frac{3}{2})$–$(3, \frac{1}{2})$ resonance.

ℓ \ m	2	3	4	5	6	7	8
5		0.1		0.2		0.1	
4			0.6		0.9		
3		0.2		3.7		0.7	
2	0.1		2.6		55.2		
1		0.5		20.7		0.7	
0	0.3		3.4		9.6		0.3

TABLE 3. $d = 3.9796$, $A = 0.075$ $E = 10^{-4}$ $\sigma = (0.14 \times 10^{-1}, -5.44)$ (truncation $[25, 9, 7]$ $M0 = 1$).

$(3, \frac{1}{2})$. This mode remains the most unstable except for a small interval centred on $A = 0.045$ where a mode 1 instability of frequency ≈ -5.44 is temporarily preferred: see table 3. The other instabilities are shown for completeness and to illustrate how the complexity of the situation develops with increasing A.

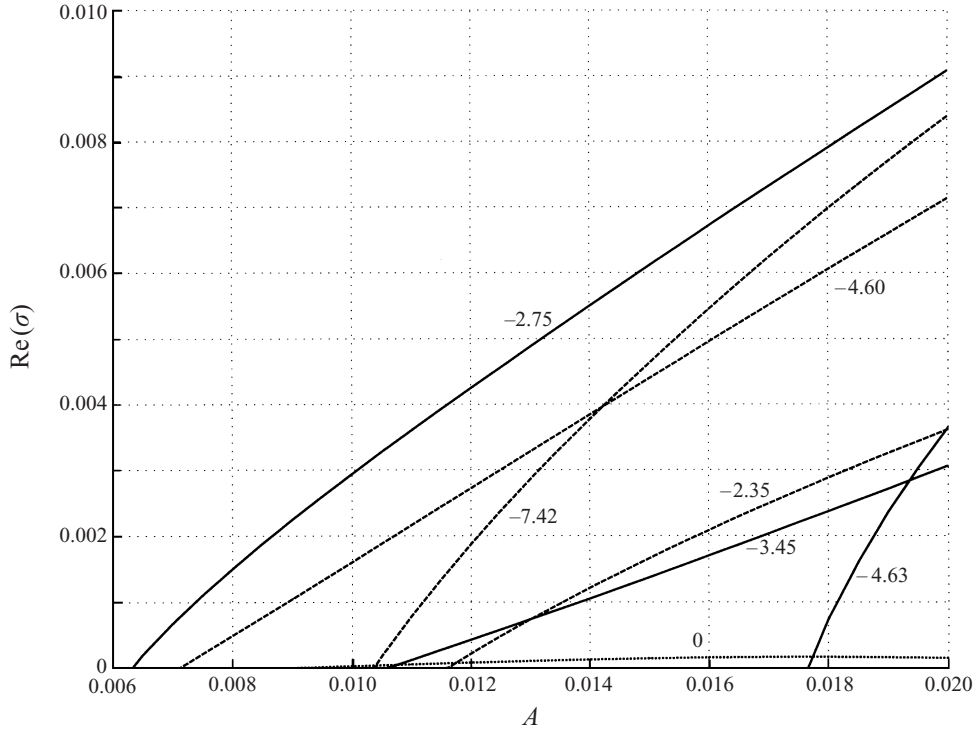

FIGURE 6. The growth rates of secondary instabilities plotted against amplitude of the underlying inertial wave for the inertial wave with $m = 1, l = 2$ in $d = 3.9796$ at $E = 10^{-5}$. The dotted line indicates modes of type 1, dashed line modes of type 2, and the solid line modes of type 3. The same dominant instability appears at this lower Ekman number.

Video footage is available of the inertial wave breakdown in this geometry (Malkus, private communication) and with it the possibility of obtaining a time-evolving frequency spectrum of the flow. Motivated by this, calculations were performed at $E = 10^{-5}$ in order to assess how robust the instability picture of figure 5 is with changing Ekman number (experiments have $E = 5 \times 10^{-5}$). Figure 6 clearly shows that the most prominent instability at $E = 10^{-4}$ is also the most unstable at $E = 10^{-5}$ (note that the critical amplitude is now down at just over 0.006! — at $E = 10^{-6}$, it is further reduced to 0.004; see the Appendix). This tentatively suggests that the $(2, \frac{3}{2})$–$(3, \frac{1}{2})$ resonance which has a frequency of $\approx 2.7/2.8$ is the most important secondary instability and should be observable in the time series data. The structures of the nearest competitor instabilities, which coincidentally are not the same as at $E = 10^{-4}$, are given in table 4.

It must be emphasized, of course, that this prediction is tentative for a number of reasons. First, we have not considered the full experimental configuration which has non-slip boundary conditions on the top and bottom surfaces rather than the stress-free conditions used here. This means that the numerically calculated growth rates will be slightly reduced in reality. Whether this additional damping actually changes the character of the most unstable instability, however, cannot be known for certain. Given the low wavenumbers of the leading instability identified here, it seems likely that the instability we have identified remains preferred. Secondly, the secondary instability analysis offered here assumes that the underlying primary inertial

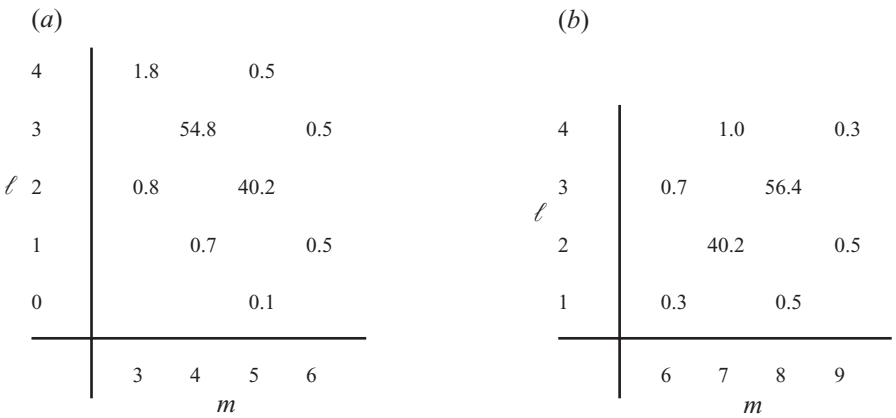

TABLE 4. $d = 3.9796$, $A = 0.02$ $E = 10^{-5}$: (*a*) $\sigma = (0.71 \times 10^{-2}, -4.60)$ (truncation $[30, 6, 5]$ $M0 = 2$) (*b*) $\sigma = (0.84 \times 10^{-2}, -7.42)$ (truncation $[30, 6, 7]$ $M0 = 4$).

wave has some steady (small) amplitude whereas in practice this wave is observed to gradually grow up to an amplitude of ≈ 0.1. Against this, the overall dominance of one secondary instability as evidenced in figures 5 and 6 over a range of amplitudes and Ekman numbers is persuasive for its importance in the breakdown observed. A final related comment is that the initial generating mechanism for the primary inertial wave has not been considered here in the interests of generality. The streamlines of the basic experimental flow (Malkus 1989) are not circular but elliptical in fact by a few percent. This distortion can excite other wave resonances subdominant to the primary inertial wave seen to grow. Whether these ultimately catch and destroy the saturated primary instability or whether secondary instabilities of the type described here are more important remains an outstanding question.

4.3. $d = 3.9796$, $E = 0$

An inviscid stability calculation was also performed for the geometry $d = 3.9796$. Figure 7 collects together all the inviscid secondary instabilities which have frequencies in the interval $(-10, 0)$ for the inertial wave amplitude $A = 0.05$. A number of the instabilities (labelled) are familiar from the viscous calculations but others are not (unlabelled). In particular, the instability with frequency -2.76 highlighted above is not obviously important, which emphasizes the limited use of the inviscid calculation in isolation.

5. Discussion

In this paper, we have presented instability results for two inertial waves which support McEwan's conjecture that an inertial wave is generically unstable to triad resonances. This resonant triad mechanism for instability demonstrated here is straightforward. In the absence of viscosity, consider a basic underlying inertial wave

$$\boldsymbol{u}_0 = \widehat{\boldsymbol{u}}_0(s)\, \mathrm{e}^{\mathrm{i}(m_0\phi + l_0\alpha z + \lambda_0 t)} \tag{5.1}$$

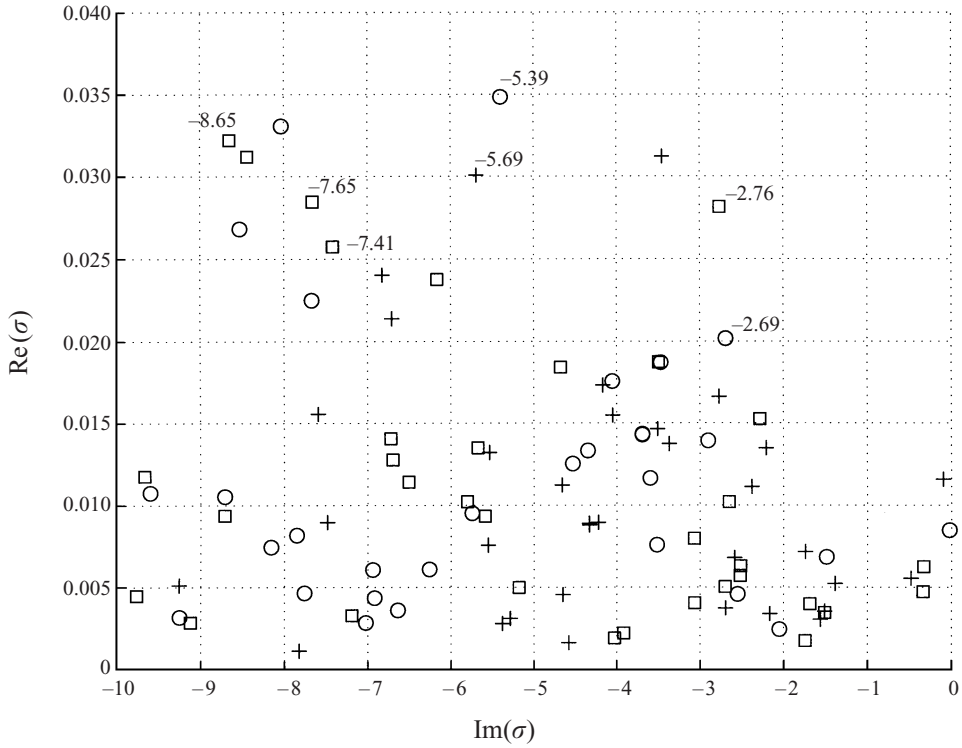

FIGURE 7. Growth rates plotted against frequencies for all secondary *inviscid* instabilities with frequencies in the interval $(-10, 0)$ for a primary inertial wave amplitude of $A = 0.05$. The circles, crosses and squares correspond to modes 1, 2 and 3 respectively. Instabilities with viscous counterparts already plotted elsewhere are labelled with a representative frequency.

and assume that this forms an exactly tuned resonant triad with the inertial waves

$$\boldsymbol{u}_1 = \widehat{\boldsymbol{u}}_1(s)\,\mathrm{e}^{\mathrm{i}(m_1\phi + l_1\alpha z + \lambda_1 t)}, \quad \boldsymbol{u}_2 = \widehat{\boldsymbol{u}}_2(s)\,\mathrm{e}^{\mathrm{i}(m_2\phi + l_2\alpha z + \lambda_2 t)}, \tag{5.2}$$

that is,

$$m_2 = m_1 + m_0, \quad \lambda_2 = \lambda_1 + \lambda_0, \quad l_2 = l_1 + l_0, \tag{5.3}$$

where all frequencies are relative to the rotating frame. In the context of this paper, the underlying inertial wave is fixed in amplitude so we have a velocity field expansion of the following form:

$$\boldsymbol{u} = A\boldsymbol{u}_0 + \epsilon\,[a(\tau)\,\boldsymbol{u}_1 + b(\tau)\boldsymbol{u}_2] + O(\epsilon A, \epsilon^2, A^2) \tag{5.4}$$

where $\tau = At$ represents the relevant slow timescale for growth. The amplitude equations for $\boldsymbol{u}_1$ and $\boldsymbol{u}_2$ are then

$$\left.\begin{aligned} \dot{a} &= \langle \boldsymbol{u}_1, \boldsymbol{u}_2{\times}(\nabla{\times}\boldsymbol{u}_0^*) + \boldsymbol{u}_0^*{\times}(\nabla{\times}\boldsymbol{u}_2)\rangle\, b, \\ \dot{b} &= \langle \boldsymbol{u}_2, \boldsymbol{u}_1{\times}(\nabla{\times}\boldsymbol{u}_0) + \boldsymbol{u}_0{\times}(\nabla{\times}\boldsymbol{u}_1)\rangle\, a, \end{aligned}\right\} \tag{5.5}$$

where $\langle \boldsymbol{u}, \boldsymbol{v}\rangle = \int\int\int \boldsymbol{u}^* \cdot \boldsymbol{v}\,\mathrm{d}V$ and the inertial waves $\boldsymbol{u}_1, \boldsymbol{u}_2$ are assumed normalized ($\langle \boldsymbol{u}_i, \boldsymbol{u}_j\rangle = \delta_{ij}$). Seeking solutions of the form $(a(\tau), b(\tau)) = (\widehat{a}, \widehat{b})\,\mathrm{e}^{\sigma\tau}$ requires

$$\sigma^2 = \left(\frac{-4\alpha^2}{\lambda_1\lambda_2}\right)\left(\frac{l_0\lambda_1 - \lambda_0 l_1}{\lambda_0}\right)^2 |\langle\, \boldsymbol{u}_1, \boldsymbol{u}_2{\times}\boldsymbol{u}_0^*\,\rangle|^2 \tag{5.6}$$

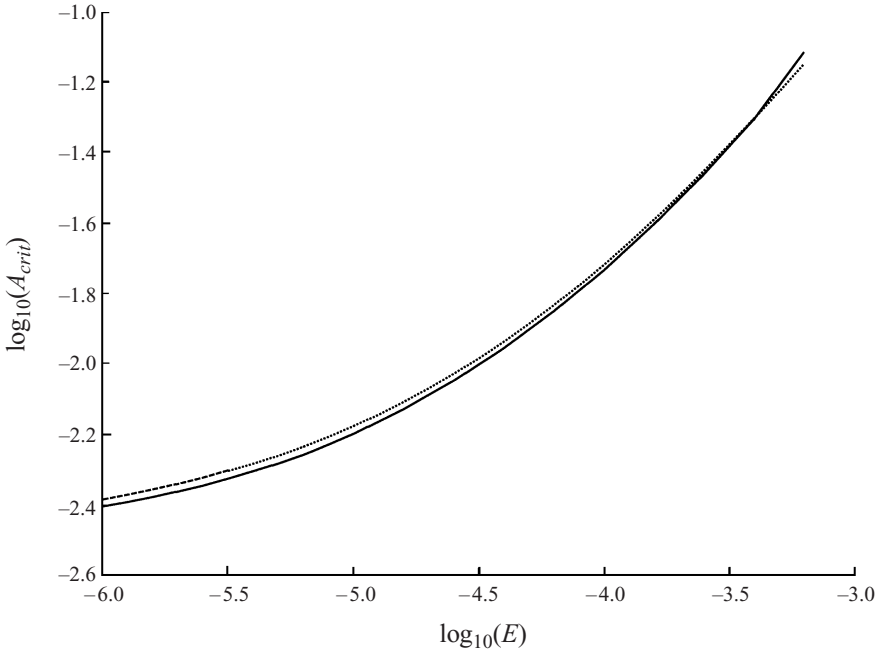

FIGURE 8. A log-log plot of how the critical amplitude for instability, A_{crit}, varies with the Ekman number E for the $(2, \frac{3}{2})$–$(3, \frac{1}{2})$ triad instability at $d = 3.9796$ (solid line). The dotted line is the asymptotic two-wave estimate given by expression (A 4). The dashed line segment shown for $10^{-6} \leqslant E \leqslant 10^{-5.5}$ is the numerical result obtained by artificially restricting the truncation to include only the two main Fourier components $(2, \frac{3}{2})$ and $(3, \frac{1}{2})$. This lies directly over the asymptotic result which has been suppressed there for clarity.

where the relation $\nabla \times \boldsymbol{u} = 2l\alpha/\lambda\, \boldsymbol{u}$ found by curling the inertial wave equation has been used to simplify the coupling elements. Instability on $O(1/A)$ timescales is assured if the frequencies λ_1 and λ_2 (in the rotating frame) are of opposite signs (and of course the coupling element does not vanish).

In reality, this instability will only occur if the amplitude of the underlying inertial wave exceeds a certain threshold value determined by the combined effects of viscous damping and frequency detuning. A calculation for the $(2, \frac{3}{2})$–$(3, \frac{1}{2})$ triad instability of §4.2 (see the Appendix) is entirely typical and illustrates that we can expect $A_{crit} = O(\Delta, E^{1/2})$ where Δ is the frequency detuning. Figure 8 contains a favourable comparison of the numerically calculated threshold amplitude for this triad instability as a function of E with the asymptotic prediction of (A 4) in the Appendix. (Figure 9 indicates the convergence with radial truncation for the $(3, \frac{1}{2})$ Fourier mode of the triad instability at $E = 10^{-5}$ and $A = 10^{-2.1}$.) The source of the small discrepancy is undoubtedly the fact that the numerical solution is still not just the two main resonating waves even down at $E = 10^{-6}$ when the threshold amplitude is $A = 0.00395$ (see the Appendix). Forcing this to be so through severe truncation produces a revised threshold curve overlaying the two-wave asymptotic prediction: see figure 8.

A priori prediction of which secondary triad instability will appear first for a growing inertial wave is fraught with difficulties. The starting point is to identify inertial wave pairings with small Δs which involves extensive numerical searching. If $\Delta \gg E^{1/2}$, which is the geophysically interesting rapid-rotation limit, choosing which of these potential triads is preferred at a given finite amplitude A then requires knowledge of

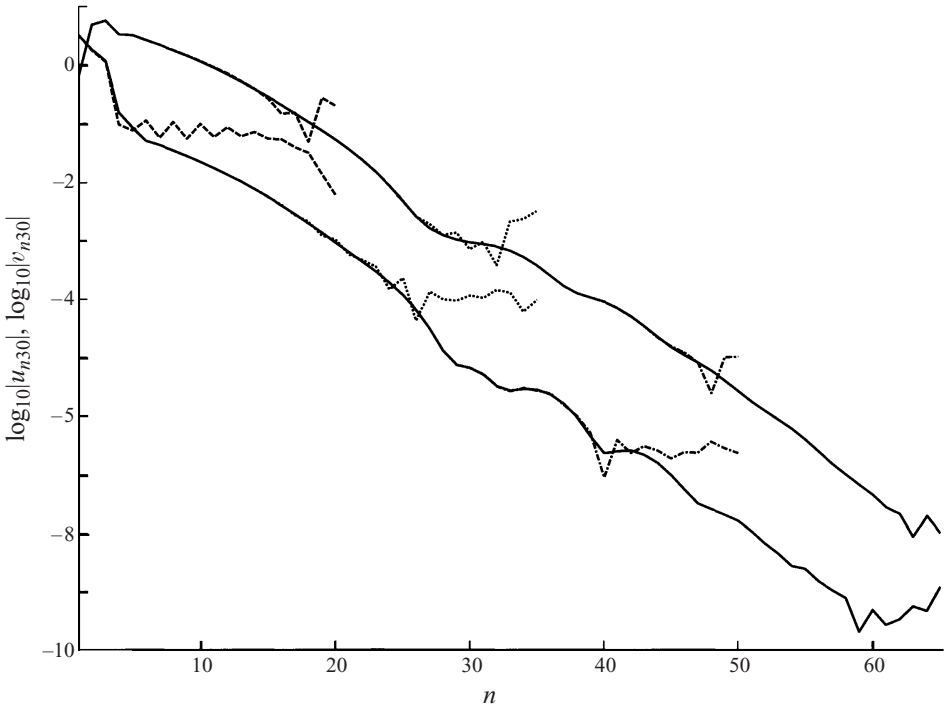

FIGURE 9. Convergence with radial truncation is illustrated here for the $(3, \frac{1}{2})$ mode of the $(2, \frac{3}{2})$–$(3, \frac{1}{2})$ triad instability. The absolute value of the spectral coefficients for the radial (lower curve) and azimuthal (upper curve) velocities, $|u_{n30}|$ and $|v_{n30}|$ (see (3.2)), are plotted on a log scale against spectral degree n at $E = 10^{-5}$ and $A = 10^{-2.1}$ for truncations (*a*) $N = 65$ (solid), (*b*) $N = 50$ (dash-dot), (*c*) $N = 35$ (dotted) and (*d*) $N = 20$ (dashed). Associated eigenvalues are as follows:

N	$\mathrm{Im}(\sigma)$	$\mathrm{Re}(\sigma)$
65	-2.74281	$+0.146207 \times 10^{-2}$
50	-2.74281	$+0.146207 \times 10^{-2}$
35	-2.74281	$+0.146244 \times 10^{-2}$
20	-2.74280	$+0.148398 \times 10^{-2}$

how strongly each pairing is coupled by the underlying inertial wave. If $\Delta = O(E^{1/2})$, which is typically the experimental situation, the presence of viscosity acts to further complicate matters by preferentially stabilizing some triads and destabilizing others through producing viscous frequency shifts which either increase or decrease Δ. Given these sorts of uncertainties, an explicit stability calculation is the safest and, in fact, may be the most efficient way to proceed. Pursuing this here has revealed surprisingly small threshold amplitudes for inertial wave instability.

We have also found an unexpected form of instability which to leading order gives rise to a geostrophic flow. This has an inviscid growth rate of $O(A^2)$ and therefore appears asymptotically subdominant to the triad instability. However, since the geostrophic instability essentially 'drives itself' through intermediary forced flows, there is not the obvious frequency tuning requirement experienced by the triad resonance mechanism. This difference means for instance that the geostrophic instability revealed in figure 2 will have a critical amplitude, A_{crit}, which scales as $O(E^{1/4})$ or $O(E^{1/2})$ depending on whether the rotating cylinder has non-slip or stress-free boundary conditions on its horizontal top and bottom surfaces respectively. In particular,

$A_{crit} \to 0$ as $E \to 0$ (for example see figure 3) whereas this is only true for a triad resonance if it is *precisely* tuned, that is $\Delta = 0$. Hence, if a geostrophic instability is present for a given inertial wave system, it will (almost) always appear before a triad if E is small enough as the underlying inertial wave grows. The fact that mean flows can grow at all upon an inertial wave has important implications for interpreting the sometimes unexpectedly 'large' mean circulations observed in rapidly rotating fluid experiments.

The cylindrical system studied here would seem particularly susceptible to secondary geostrophic instabilities because of its well-known degeneracy of geostrophic contours. Essentially, any m-component of the two-dimensional geostrophic flow $\boldsymbol{u}_G(s,\phi) = \sum_m [u_G^{(m)}(s)\widehat{\boldsymbol{s}} + v_G^{(m)}(s)\widehat{\boldsymbol{\phi}}]\,\mathrm{e}^{\mathrm{i}m\phi}$ can individually become unstable whereas in a sphere, for example, the geostrophic flow is only one-dimensional, $\boldsymbol{u}_G(s) = v_G(s)\widehat{\boldsymbol{\phi}}$. Thus there appears less opportunity for this type of instability to manifest itself in the geophysically interesting spherical case. Nevertheless, the fact that these instabilities, which are almost steady *in the rotating frame*, exist at all has importance for recent studies suggesting that inertial waves may be excited in the Earth's outer core (Aldridge & Lumb 1987; Aldridge, Lumb & Henderson 1989; Aldridge *et al.* 1997; Kerswell 1993, 1994). Here the outstanding question is whether diurnal (daily) forcing by tidal and precessional effects can lead to long (Ohmic diffusion) timescale dynamics within the outer core. Growth rates of the primary inertial waves on Ohmic diffusion timescales (Kerswell 1994) already provides one possible route to long-term dynamics. Secondary instabilities consisting of almost steady geostrophic flows may provide another.

The author gratefully acknowledges the support of The Royal Society and would like to thank a referee for particularly careful comments.

Appendix. The $(2, \frac{3}{2})$–$(3, \frac{1}{2})$ resonance

We can attempt to understand the $(2, \frac{3}{2})$–$(3, \frac{1}{2})$ resonance observed in the numerical calculations by adopting a two-wave expansion of the perturbed velocity field:

$$\boldsymbol{u} = s\widehat{\boldsymbol{\phi}} + \mathscr{U}(\boldsymbol{x}) + a\boldsymbol{Q}_1(s)\,\mathrm{e}^{2\mathrm{i}\phi + \frac{3}{2}\mathrm{i}\alpha z + \sigma t} + b\boldsymbol{Q}_2(s)\,\mathrm{e}^{3\mathrm{i}\phi + \frac{1}{2}\mathrm{i}\alpha z + \sigma t}. \tag{A 1}$$

Here $\boldsymbol{Q}_1(s)$ and $\boldsymbol{Q}_2(s)$ give the velocity structure of the $(2, \frac{3}{2})$ and $(3, \frac{1}{2})$ inertial waves and $\mathscr{U}$ is the finite-amplitude primary inertial mode. These would seem to be the leading terms of an asymptotic expansion of the velocity field in the limit of the spinover amplitude $A \to 0$. However, inviscid detuning of the two inertial waves means that A has a minimum finite value for the resonance to be marginally stable and therefore this limit is unavailable. Instead we have what is in effect a Galerkin truncation where the neglected terms are $O(A)$ smaller than the retained ones. Working typically at $E = 10^{-6}$ where $A_{crit} = O(0.004)$, this is a reasonable approximation.

Substituting the expansion (A 1) into the Navier–Stokes equation and projecting onto $\boldsymbol{Q}_1$ and $\boldsymbol{Q}_2$ respectively gives

$$\left.\begin{aligned} \left[\sigma - (\mathrm{i}\lambda_1 + s_1 E^{1/2})\right] a &= -\mathrm{i}AC_1\, b, \\ \left[\sigma - (\mathrm{i}\lambda_2 + s_2 E^{1/2})\right] b &= +\mathrm{i}AC_2\, a, \end{aligned}\right\} \tag{A 2}$$

where

$$-\mathrm{i}AC_1\, b = \frac{\langle \boldsymbol{Q}_1^* \cdot (-\boldsymbol{u}\cdot\nabla\mathscr{U} - \mathscr{U}\cdot\nabla\boldsymbol{u})\rangle}{\langle \boldsymbol{Q}_1^* \cdot \boldsymbol{Q}_1\rangle}, \quad \mathrm{i}AC_2\, a = \frac{\langle \boldsymbol{Q}_2^* \cdot (-\boldsymbol{u}\cdot\nabla\mathscr{U} - \mathscr{U}\cdot\nabla\boldsymbol{u})\rangle}{\langle \boldsymbol{Q}_2^* \cdot \boldsymbol{Q}_2\rangle}, \tag{A 3}$$

Inertial wave	$(2, \frac{3}{2})$		$(3, \frac{1}{2})$	
E	s_1^i	s_1^r	s_2^i	s_2^r
$\downarrow 0$	0.4875	−0.4875	−0.3665	−0.3665
10^{-8}	0.4875	−0.4916	−0.3665	−0.3703
$10^{-7.5}$	0.4875	−0.4949	−0.3665	−0.3733
10^{-7}	0.4875	−0.5006	−0.3665	−0.3787
$10^{-6.5}$	0.4875	−0.5108	−0.3665	−0.3882
10^{-6}	0.4875	−0.5289	−0.3664	−0.4051
$10^{-5.5}$	0.4875	−0.5612	−0.3663	−0.4353
10^{-5}	0.4876	−0.6187	−0.3659	−0.4890
$10^{-4.5}$	0.4876	−0.7211	−0.3647	−0.5851
10^{-4}	0.4850	−0.9041	−0.3608	−0.7579

TABLE 5. Numerically calculated viscous frequency corrections to the inertial waves $(2, \frac{3}{2})$ and $(3, \frac{1}{2})$ which have frequencies ≈ -2.74 in the laboratory frame of a rotating cylinder with height-to-radius ratio of $d = 3.9796$. The frequency of $(2, \frac{3}{2})$ is $-2.740531976 + (s_1^i - is_1^r)E^{1/2}$ and $-2.744064679 + (s_2^i - is_2^r)E^{1/2}$ for $(3, \frac{1}{2})$. The theoretical asymptotic values are entered in the row labelled with $\downarrow 0$.

ℓ \ m	1	2	3	4
2.5	0.015	0.000	0.002	0.000
1.5	0.000	69.428	0.000	0.000
0.5	0.004	0.003	30.547	0.001

TABLE 6. The structure of the $(2, \frac{3}{2})$–$(3, \frac{1}{2})$ resonance at $E = 10^{-6}$ and $A = 0.00395$ where $\sigma_r \approx 0$, $\sigma_i = 2.742636028$) (truncation $[55, 3, 2]$ $M0 = 1$). Figures shown represent % energy in each Fourier component.

$\langle\ \rangle = \int\int\int \mathrm{d}V$, the inviscid frequencies $\lambda_1 = -2.740531976$ and $\lambda_2 = -2.744064679$, and $s_1 = s_1^r + \mathrm{i}s_1^i$ and $s_2 = s_2^r + \mathrm{i}s_2^i$ are the viscous (complex) frequency shifts for each inertial wave (Greenspan 1969). For non-trivial solutions (a, b) at criticality $\mathrm{Re}(\sigma) = \sigma_r = 0$, we find that

$$\left.\begin{aligned} \mathrm{Im}(\sigma) = \sigma_i &= \frac{s_1^r(\lambda_2 + s_2^i E^{1/2}) + s_2^r(\lambda_1 + s_1^i E^{1/2})}{s_1^r + s_2^r}, \\ A_{crit} &= \left(\frac{E s_1^r s_2^r}{C_1 C_2}\left[\frac{E(s_1^r + s_2^r)^2 + (\lambda_2 + s_2^i E^{1/2} - \lambda_1 - s_1^i E^{1/2})^2}{E(s_1^r + s_2^r)^2}\right]\right)^{1/2}. \end{aligned}\right\} \tag{A 4}$$

Loosely speaking, $A_{crit} = O(\Delta, E^{1/2})$ where $\Delta = \lambda_2 + s_2^i E^{1/2} - \lambda_1 - s_1^i E^{1/2}$ is the frequency detuning. Table 5 and figure 10 indicate how the viscous frequency corrections, s_1 and s_2, of the two inertial waves vary with Ekman number. There is clearly convergence to the theoretical asymptotic values (Kerswell & Barenghi 1995, equation (2.12) with $d \to \infty$) as $E \to 0$ but even at $E = 10^{-6}$ the difference between actual and asymptotic

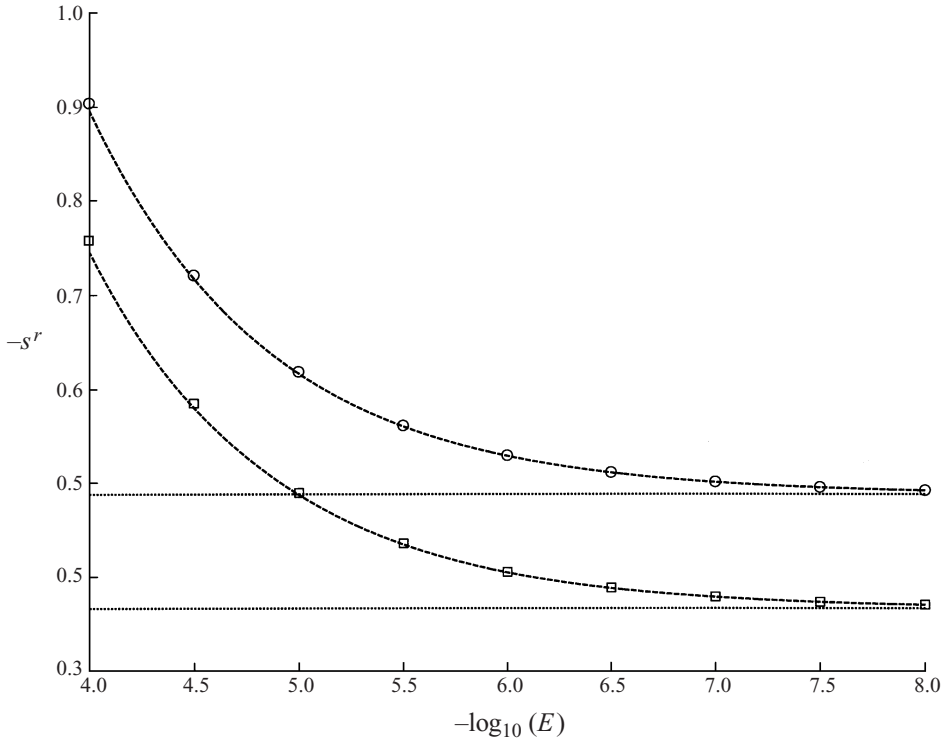

FIGURE 10. Viscous decay rates s_1^r and s_2^r are plotted against $-\log_{10} E$ for the two inertial waves which constitute the most unstable instability of the primary inertial wave. The upper dotted line indicates the standard asymptotic result -0.4875 for mode $(2, \frac{3}{2})$ and the circles are numerical data points. The upper dashed line appearing to go through them is found by incorporating the interior dissipation contribution, that is, $s_1^r \approx -0.4875 - (k_1^2 + (\frac{3}{2}\alpha)^2)E^{1/2}$ ($k_1 = 5.9415$). Similarly the lower dotted line is the asymptotic result -0.3665 for the mode $(3, \frac{1}{2})$ with squares marking the numerical data points being and the lower dashed line is $s_2^r = -0.3665 - (k_2^2 + (\frac{1}{2}\alpha)^2)E^{1/2}$ ($k_2 = 6.1182$).

values is still about 10%. Incorporating the $O(E)$ interior dissipation contribution, $\mathrm{i}(k^2 + \ell^2\alpha^2)E$, into the frequency resolves this discrepancy (see figure 10) and is therefore used to evaluate A_{crit} in (A 4) (C_1C_2 is 0.28591). Figure 8 compares the numerical A_{crit} with the two-wave asymptotic prediction of (A 4). The discrepancy between the curves is due to the fact that the numerical solution involves more than just the two main Fourier modes $(2, \frac{3}{2})$ and $(3, \frac{1}{2})$ even at Ekman numbers of $E = 10^{-6}$ where the critical amplitude is $A = 0.00395$: see table 6. Artificially restricting the numerical solution to just the two main Fourier components $(2, \frac{3}{2})$ and $(3, \frac{1}{2})$ (by choosing the truncation $[55, 1, 1]$ $M0 = 2$), the critical amplitude curve, shown as the dashed line segment of figure 8, then overlays the asymptotic prediction.

REFERENCES

ALDRIDGE, K. D. & LUMB, L. I. 1987 Inertial waves identified in the Earth's fluid outer core. *Nature* **325**, 421–423.

ALDRIDGE, K. D., LUMB, L. I. & HENDERSON, G. A. 1989 A Poincaré model for the Earth's fluid core. *Geophys. Astrophys. Fluid Dyn.* **48**, 5–23.

ALDRIDGE, K., SEYED-MAHMOUD, B., HENDERSON, G. & WIJNGAARDEN, W. VAN 1997 Elliptical instability of the Earth's fluid core. *Phys. Earth Planet. Inter.* **103**, 365–374.

ALDRIDGE, K. D. & TOOMRE, A. 1969 Inertial oscillations of a rotating fluid sphere. *J. Fluid Mech.* **37**, 307–323.

BAINES, P. G. 1967 Forced oscillations of an enclosed rotating fluid. *J. Fluid Mech.* **30**, 533–546.

BJERKNES, V., BJERKNES, J., SOLBERG, H. & BERGERON, T. 1933 *Physikalische Hydrodynamik*, pp. 465–471. Springer.

BUSSE, FH. 1968 Steady fluid flow in a precessing spheroidal shell. *J. Fluid Mech.* **33**, 739–752.

CARTAN, E. 1922 Sur les petites oscillations d'une masse fluid. *Bull. Sci. Math.* **46**, 317–352, 356-369.

FABIJONAS, B., HOLM, D. D. & LIFSCHITZ, A. 1997 Secondary instabilities of flows with elliptic streamlines. *Phys. Rev. Lett.* **78**, 1900–1903.

FULTZ, D. 1959 A note on overstability, and the elastoid-inertia oscillations of Kelvin, Solberg and Bjerknes. *J. Met.* **16**, 199–208.

GANS, R. F. 1970 On the precession of a resonant cylinder. *J. Fluid Mech.* **41**, 865–872.

GLEDZER, YE. B., NOVIBOV, YU. V, OBUKHOV, A. M. & CHUSOV, M. A. 1974 An investigation of the stability of liquid flows in a three-axis ellipsoid. *Isv. Atmos. Ocean. Phys.* **10**, 69–71.

GLEDZER, E. B. & PONOMAREV, V. M. 1977 Finite-dimensional approximation of the motions of an incompressible fluid in an ellipsoidal cavity. *Isv. Atmos. Ocean. Phys.* **13**, 565–569.

GLEDZER, E. B. & PONOMAREV, V. M. 1992 Instability of bounded flows with elliptical streamlines. *J. Fluid Mech.* **240**, 1–30.

GREENSPAN, H. P. 1968 *The Theory of Rotating Fluids.* Cambridge University Press (reprinted Breukelen Press 1990).

GREENSPAN, H. P. 1969 On the non-linear interaction of inertial modes. *J. Fluid Mech.* **36**, 257–264.

HOLLERBACH, R. & KERSWELL, R. R. 1995 Oscillatory internal shear layers in rotating and precessing flows. *J. Fluid Mech.* **298**, 327–339.

JOHNSON, L. E. 1967 The precessing cylinder. In *Notes on the 1967 Summer Study Program in Geophysical Fluid Dynamics at the Woods Hole Oceanographic Inst*. Ref. 67-54, pp. 85–108.

KELVIN, LORD 1880 Vibrations of a columnar vortex. *Phil. Mag.* **10**, 155–168.

KERSWELL, R. R. 1993 The instability of precessing flow. *Geophys. Astrophys. Fluid Dyn.* **72**, 107–144.

KERSWELL, R. R. 1994 Tidal excitation of hydromagnetic waves and their damping in the Earth. *J. Fluid Mech.* **274**, 219–241.

KERSWELL, R. R. 1995 On the internal shear layers spawned by the critical regions in oscillatory Ekman boundary layers. *J. Fluid Mech.* **298**, 311–325.

KERSWELL, R. R. & BARENGHI, C. F. 1995 On the viscous decay rates of inertial waves in a rotating circular cylinder. *J. Fluid Mech.* **285**, 203–214.

KERSWELL, R. R. & DAVEY, A. 1996 On the linear instability of elliptic pipe flow. *J. Fluid Mech.* **316**, 307–324.

KERSWELL, R. R. & MALKUS, W. V. R. 1998 Tidal instability as the source for Io's magnetic signature. *Geophys. Res. Lett.* **25**, 603–606.

KOBINE, J. J. 1995 Inertial wave dynamics in a rotating and precessing cylinder. *J. Fluid Mech.* **303**, 233–252.

KOBINE, J. J. 1996 Azimuthal flow associated with inertial wave resonance in a precessing cylinder. *J. Fluid Mech.* **319**, 387–406.

LIFSCHITZ, A. & FABIJONAS, B. 1996 A new class of instabilities of rotating fluids. *Phys. Fluids* **8**, 2239–2241.

MALKUS, W. V. R. 1968 Precession of the Earth as the cause of geomagnetism. *Science* **160**, 259–264.

MALKUS, W. V. R. 1989 An experimental study of the global instabilities due to the tidal (elliptical) distortion of a rotating elastic cylinder. *Geophys. Astrophys. Fluid Dyn.* **48**, 123–134.

MALKUS, W. V. R. 1994 Energy sources for planetary dynamos. In *Theory of Solar and Planetary Dynamos*. NATO ASI Conference Series, Cambridge University Press.

MALKUS, W. V. R. & WALEFFE, F. A. 1991 Transition from order to disorder in elliptical flow: a direct path to shear flow turbulence. In *Advances in Turbulence 3* (ed. A. V. Johansson & P. H. Alfredsson), pp. 197–203.

MANASSEH, R. 1992 Breakdown regimes of inertia waves in a precessing cylinder. *J. Fluid Mech.* **243**, 261–296.

MANASSEH, R. 1994 Distortions of inertia waves in a rotating fluid cylinder forced near its fundamental mode resonance. *J. Fluid Mech.* **265**, 345–370.

MANASSEH, R. 1996 Nonlinear behaviour of contained inertia waves. *J. Fluid Mech.* **315**, 151–173.

Mason, D. M. & Kerswell, R. R. 1998 Nonlinear evolution of the elliptical instability. (In preparation).

McEwan, A. D. 1970 Inertial oscillations in a rotating fluid cylinder. *J. Fluid Mech.* **40**, 603–640.

Newhouse, S., Ruelle, D. & Takens, F. 1978 Occurrence of Strange Axiom A Attractors near quasiperiodic flows on T^m, $m \geqslant 3$. *Commun. Math. Phys.* **64**, 35–40.

O'Sullivan, P. L. & Breuer, K. S. 1994 Transient growth in circular pipe flow. I. Linear disturbances. *Phys. Fluids* **6**, 3643–3651.

Poincaré, H. 1910 Sur la précession des corps déformables. *Bull. Astronomique* **27**, 321–356.

Rieutord, M. 1991 Linear theory of rotating fluids using spherical harmonics part II, time-periodic flows. *Geophys. Astrophys. Fluid Dyn.* **59**, 185–208.

Ruelle, D. & Takens, F. 1971 On the nature of turbulence. *Commun. Math. Phys.* **20**, 167–192.

Stergiopoulos, S. & Aldridge, K. D. 1982 Inertial waves in a fluid partially filling a cylindrical cavity during spin-up from rest. *Geophys. Astrophys. Fluid Dyn.* **21**, 89–112.

Stergiopoulos, S. & Aldridge, K. D. 1987 Ringdown of inertial waves during spin-up from rest of a fluid contained in a rotating cylindrical cavity. *Phys. Fluids* **30**, 302–311.

Tilgner, A. 1998 Driven inertial oscillations in spherical shells. *Preprint*.

Vladimirov, V. A. & Tarasov, V. 1985 Resonance instability of the flows with closed streamlines. In *Laminar-Turbulent Transition; IUTAM Symp., Novosibirsk, 1984* (ed. V. V. Kozlov), pp. 717–722. Springer.

Vladimirov, V. A. & Vostretsov, D. 1986 Instability of steady flows with constant vorticity in vessels of elliptic cross-section. *Prikl. Matem. Mekhan.* **50**(3), 367–377. (Transl. *J. Appl. Math. Mech.* **50**(3), 369–377.)

Waleffe, F. A. 1989 The 3D instability of a strained vortex and its relation to turbulence. PhD thesis, MIT.